Biophysical Journal, Volume *113*

Supplemental Information

The Detection of Nanoscale Membrane Bending with Polarized Localization Microscopy

Abir M. Kabbani and Christopher V. Kelly

SUPPLEMENTAL INFORMATION for

The detection of nanoscale membrane bending with polarized localization microscopy

A. M. Kabbani and C. V. Kelly

Supported lipid bilayer formation

Giant unilamellar vesicles (GUVs) of primarily 1-palmitoyl-2-oleoyl-sn-glycero-3-phosphocholine (POPC, Avanti Polar Lipids, Inc.) labeled with 0.3 mol% 1,1'-didodecyl-3,3,3',3'-tetramethylindocarbocyanine perchlorate (DiI, Life Technologies) were prepared by electro-formation, as described previously (1). This fluorophore density yielded 110 nm^2 of bilayer per DiI molecule. In brief, GUVs were formed by mixing lipids in chloroform and spreading them uniformly on a conducting indium tin oxide (ITO)-coated slide (Sigma-Aldrich) via spin coating. The resulting lipid film was dried under vacuum for >20 min. A second ITO-coated slide and silicon spacer enclosed the dried lipids into an incubation chamber. A hydration solution of 200 mM sucrose was added to the dried lipid films and the ITO slides were connected to a sine wave function generator. The growth of the GUVs occurred over 3 hours at 55 °C with an alternating voltage of 10 Hz and 2 V_{rms}. GUVs were stored at 55 °C and discarded after 3 days. GUVs were created varying in diameter from <200 nm through 100 μm. The GUVs were placed on the glass bottom dishes and the NPs for up to 1 hour at room temperature. The interaction between the GUVs with the plasma cleaned glass coverslip resulted in bursting of the GUVs and the formation of patches of SLB over the glass and NPs. This method of SLB creation proved to create more uniform SLBs over the NPs than SLBs formed by the fusion of large unilamellar vesicles (LUVs).

Large unilamellar vesicles (LUVs) preparation

POPC, DiI and occasionally DPPE-Biotin in chloroform were mixing in a glass vial. DiI was added to 0.3 mol% of all lipids, DPPE-Biotin was occasionally added to 1 mol% of all lipids, and POPC was the remaining >98.7 mol%. The mixture was dried under nitrogen gas and placed under vacuum >20 min. The lipid films were hydrated in 1X PBS buffer to a concentration of 1 mg/L. The sample was vortexed, pre-extruded once through a polycarbonate

membrane filter of 400 nm pore size, and extruded 20 times through a membrane filter of 100 nm pore size. 5 μL of 10 mM CaCl2 and 120 μL of 1 mg/L LUVs were added to a cleaned MatTek dish and incubated for 30 min. Excess LUVs were washed away with PBS buffer. When DPPE-Biotin was included, 20 μL of 50 μg/mL of streptavidin solution was added to immobilize the remaining unfused LUVs to the underlying SLB.

Imaging buffer

PLM was performed on samples present in an oxygen-scavenging buffer (2, 3) (150 mM NaCl, 50 mM TRIS, 0.5 mg/mL glucose oxidase, 20 mg/mL glucose, and 40 μg/mL catalase at pH 8). Buffer proteins were purchased from Sigma-Aldrich and salts were purchased from Fisher Scientific. These conditions maintain a low free oxygen concentration in the buffer to minimize non-reversible fluorophore bleaching and encourage transient fluorophore blinking, as is necessary for SMLM.

Polarization confirmation after passing through TIRF objective

The intensity of the p- and s-polarized light were separately measured versus applied voltage to the liquid crystal wave plate (LCWP). The 561 nm laser was passed through the liquid crystal wave plate and through the TIRF microscope objective with an existing angle of 65°, as would be the case for PLM. After the objective, the laser passed through a linear polarizer (LPVISE100-A, Extinction ratio: 18000:1, Thorlabs, Inc.) in either a vertical or horizontal orientation prior to being incident on a power meter (PM100D, Thorlabs, Inc.). After transmitting through the LCWP, the microscope objective, and the linear polarizer, the laser power was measured while sweeping through voltages to the LCWP with a custom-made LabVIEW program. The power ratios of the P/S and S/P are plotted in Fig. S2. At the optimal voltages of 1.924 and 1.245 V, the power ratio of P/S and S/P are 207:1 and 54:1, respectively. These ratios were approximated as infinite for the theoretical analysis in this manuscript.

Data analysis calculations

Signal-to-noise calculations of diffraction-limited images were performed by taking the ratio of the mean intensity difference at the membrane bud divided by the standard deviation of the intensity of the surrounding planar SLB. Whereas, the signal-to-noise ratio (SNR) for the

super-resolution reconstructed images was evaluated through dividing the mean signal, calculated from the number of localizations at the curvature location, by the standard deviation of the number of localizations of the flat bilayer.

The size of each membrane bud (<*r*>) was set equal to the mean distance from the bud center of all extra localizations due to the bud. This was calculated by taking into consideration the background from flat SLB localizations of uniform density (ρ), the distance of each localization from the bud center (r_i), and a threshold distance that was significantly greater than <*r*> (*R*). Typically, *R* = 400 nm but the following calculation is independent of the particular *R* chosen. The number of extra localizations due to the presence of the bud (N_{bud}) is equal to the total number of localizations (N_{all}) within $r_i < R$ subtracted from the number of localizations expected within *R* if no bud was present (N_{SLB}); $N_{SLB} = \pi R^2 \rho = N_{all} - N_{bud}$. The mean r_i expected for the flat SLB within *R* is 2*R*/3. By analyzing all collected localizations within *R* and subtracting the expected localizations from the flat SLB, <*r*> is calculated according to

$$< r >= \frac{\sum r_i}{N_{bud}} - \frac{2\pi\rho R^3}{3N_{bud}}. \qquad \text{(Eq. S1)}$$

Simulated error in image reconstruction of diffusion

The distribution of localizations around the nanoparticle-induced membrane buds was influenced by multiple effects that limit the experimental determination of the membrane topography, including (1) localization imprecision of the individual fluorophores, (2) anisotropic emission from the membrane-confined DiI, (3) finite localization rates, (4) NP-induced emission lensing, (5) the fitting of multiple 'on' fluorophores as if they were a single fluorophore, and (6) membrane curvature motion within the sample (i.e., NP or LUV drift) (Fig. S12). The simulations over the membrane topography resulted in the *x*, *y*, and *z* location of the single lipids versus simulation time (t_s).

A random distribution of discrete points was created over the simulated membrane topography by a Monte-Carlo method (Fig. 5C) with an average density of 1 point/nm^2. A simulated single lipid was allowed to randomly step between points. Single simulations steps were equivalent to 3.1 μs and 2.6 nm to mimic a diffusion coefficient of 0.55 μm^2/s. The simulated lipid positions, separated by 6400 simulation steps, were compared to mimic a 50 Hz camera frame rate to match experimental data. Whereas the experimental data incorporated

camera blur and t_{exp} of 18 ms, simulated positions had an equivalent t_{exp} = 0 and no camera blur. 7,800 steps were simulated and considered in the diffusion analysis over the curved membrane.

To mimic the local change in membrane viscosity due to curvature exhibited as an apparent slowing in the lipid diffusion, the effective time per simulation step was modified. Single simulations steps on the flat membrane were kept equivalent to 3.1 μs and 2.6 nm, while these values changed to (3.1*D_{ratio}) μs for each 2.6 nm when the simulated lipid was on the curved membrane. This enabled simulation the slowing of lipids by a factor of D_{ratio} on the curved membrane compared to the flat bilayer. In the absence of simulated error, the step lengths (v) were calculated as

$$v(t_S) = \sqrt{(x(t_s) - x(t_s + 6400))^2 + (y(t_s) - y(t_s + 6400))^2} \quad \text{(Eq. S2)}$$

and the distribution of v was used to fit Eq. 1.

(1) When a localization imprecision of $\sigma_r^2 = 2\sigma_{xy}^2$ was incorporated into the simulations, a normal distribution of random numbers with a standard deviation of σ_{xy} (Σ) was used and the simulated step lengths were calculated as

$$v(t_S) = \sqrt{(x(t_s) - x(t_s + 6400) + 2\Sigma)^2 + (y(t_s) - y(t_s + 6400) + 2\Sigma)^2} \quad \text{(Eq. S3)}$$

(2) Anisotropic emission contributed to the single lipids being localized at a location distinct from their true location dependent on the orientation and height of the membrane. The effects of rotationally confined fluorophores can yield lateral localization inaccuracies up to 100 nm upon defocusing by 200 nm (4). Numerical integration yielded the magnitude and direction of the shift in localization position due to the single fluorophore orientation and height above the focal plane following the framework of Agrawal et al. (5). The expected PSF and lateral shift were estimated as a function of membrane orientation (θ and φ) after considering the expected fluorophore orientations within the membrane (ψ and β). Accordingly, the expected lateral shifts as a function of membrane orientation and height were calculated. This systematic shift was incorporated into our simulated image reconstruction and SPT results, proving to be critical for matching the experimental data. Since the magnitude of the anisotropic emission effects varies greatly with the distance between the single fluorophore in the membrane and the focal plane, and since this distance was difficult to experimentally assess, the magnitude of defocusing and

lateral shifting was fit to match experimental and theoretical results. From this, a perceived location was calculated for each lipid location at each simulated time and the step lengths were calculated as described above from the perceived locations.

(3) The finite localization rates result in a finite number of localizations per membrane budding event. With greater localizations, greater precision could be gained in detecting the center of the membrane bud, the local membrane orientation, the radial density of localizations, and the spatial mapping of the lipid diffusion rate.

(4) Nanoparticle-induced lensing has the potential to cause a systematic shift in the perceived location of a fluorophore from its actual position, similar to the anisotropic emission effects. Lensing effects were coarsely estimated by considering the ray trajectories leaving a point source in water that was 5 nm away from the polystyrene nanoparticle and imaged by a thin lens. The changes in the index of refraction from the water, the polystyrene, and the coverslip yielded a slight shifting of the point spread function such that the nanoparticle lensing shifted the single-fluorophore images towards the center of the nanoparticle on the imaging plane. However, this effect was of lower magnitude than the anisotropic emission and unneeded to reproduce the experimental data.

(5) When performing SMLM, such as PLM, a key component of data analysis is the fitting of single-fluorophore images. When two fluorophores are '*on*' and treated as a single fluorophore's image, errors will result in the data analysis and interpretation. With pPLM, the fluorophores on the membrane that are parallel to the coverslip, which is most of the membrane, are less likely to be excited and less likely to be turned '*off*' than with s-polarized illumination. Accordingly, it would be expected to have a higher concentration of '*on*' fluorophores during pPLM than sPLM. This higher concentration of '*on*' fluorophores coupled with the increased probability of detecting fluorophores when they are on the sub-diffraction-limited membrane bud, would increase the probability that raw pPLM images would be more likely to yield multiple '*on*' fluorophores simultaneously on the membrane bud than raw sPLM images. If multiple '*on*' fluorophores were fit as a single fluorophore, the resulting fit center would be biased towards the center of the membrane bud. This effect was simulated by considering a Poissonian distribution of fluorophores simultaneously '*on*' on the bud. As expected, by increasing the number of simultaneously '*on*' fluorophores, the distribution of localizations

became higher near the bud center. However, this effect proved to be unnecessary to reproduce the experimental data.

(6) Error in localizing the center of the membrane bud (σ_b) results in error determining the lipid behaviors versus distance from the bud center (r). In the simulations, r for a single lipid step was calculated according to

$$r(t) = \frac{1}{2}\sqrt{(x(t_s) + x(t_s + 6400) + \sigma_b)^2 + \big(y(t_s) + y(t_s + 6400)\big)^2} \qquad \text{(Eq. S4)}$$

As described in the manuscript, σ_b was experimentally equal to 3 ± 1 nm and this value was put into the simulations of D_{xy} versus r. In some experimental conditions, the membrane bud was observed moving over time and this could be incorporated into the simulation by allowing σ_b to have a time dependence and/or fluctuation in the analysis of the simulation results.

SUPPLEMENTAL FIGURES

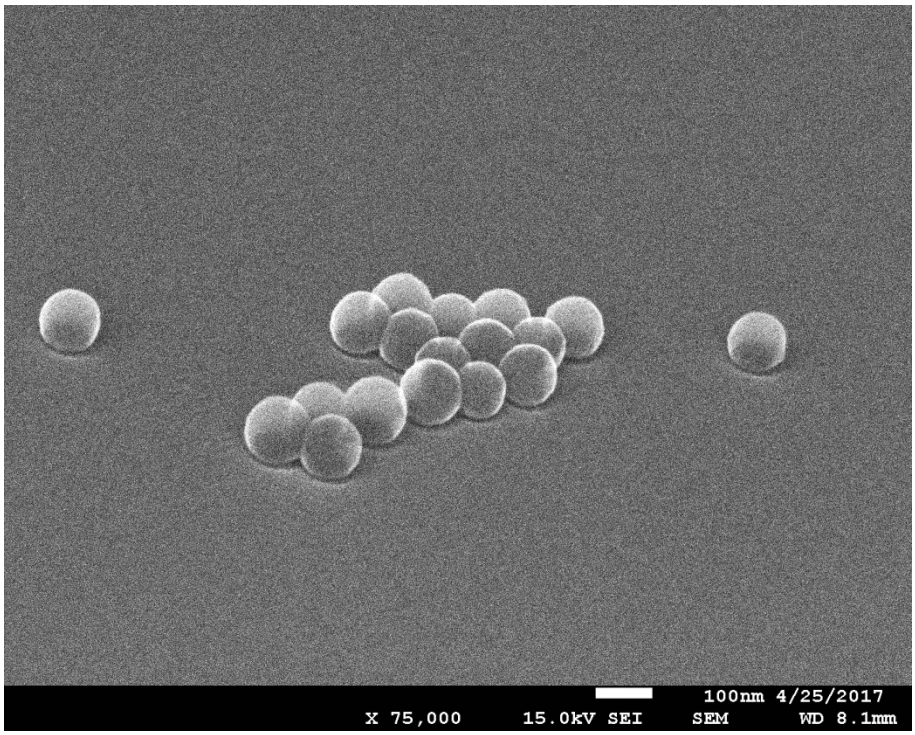

FIGURE S1 To confirm the fidelity of the nanoparticles shape, structure, and size after exposure to the hotplate, scanning electron microscope (SEM) images were then acquired using a field emission scanning electron microscopy (JSM-7600F from Jeol USA, Inc.) in the Wayne State University Electron Microscopy Laboratory. These 51 nm diameter polystyrene nanoparticles were carbon coated and imaged at an angle of 55° with a secondary electron detector to reveal the heights of the nanoparticles from the coverslip.

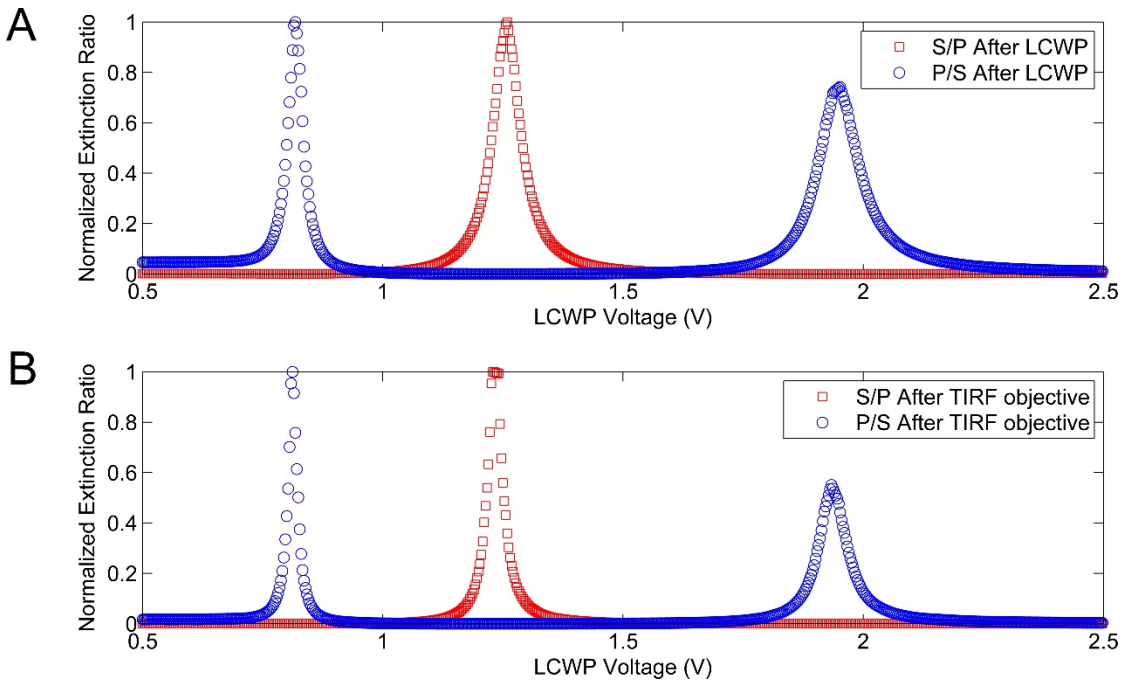

FIGURE S2 The extinction ratio of p-polarized and s-polarized excitation light after passing through the liquid crystal and the TIRF objective demonstrates the uncompromised polarization of light after passing through the two optical components. The chosen voltages to perform PLM for the two polarizations show the high extinction ratio for P/S and S/P for p-polarized and s-polarized light, respectively. The ratio of output powers at a range of voltages after passing through (A) the liquid crystal wave plate, and (B) the TIRF objective are plotted. The ratios of the eventual p-polarization to s-polarization after passing through the liquid crystal are: P/S = 68:1 and S/P = 135:1. The ratios of the p-polarization to s-polarization after passing through the TIRF objective are: P/S = 207:1 and S/P = 54:1 when the appropriate voltages were applied to the liquid crystal.

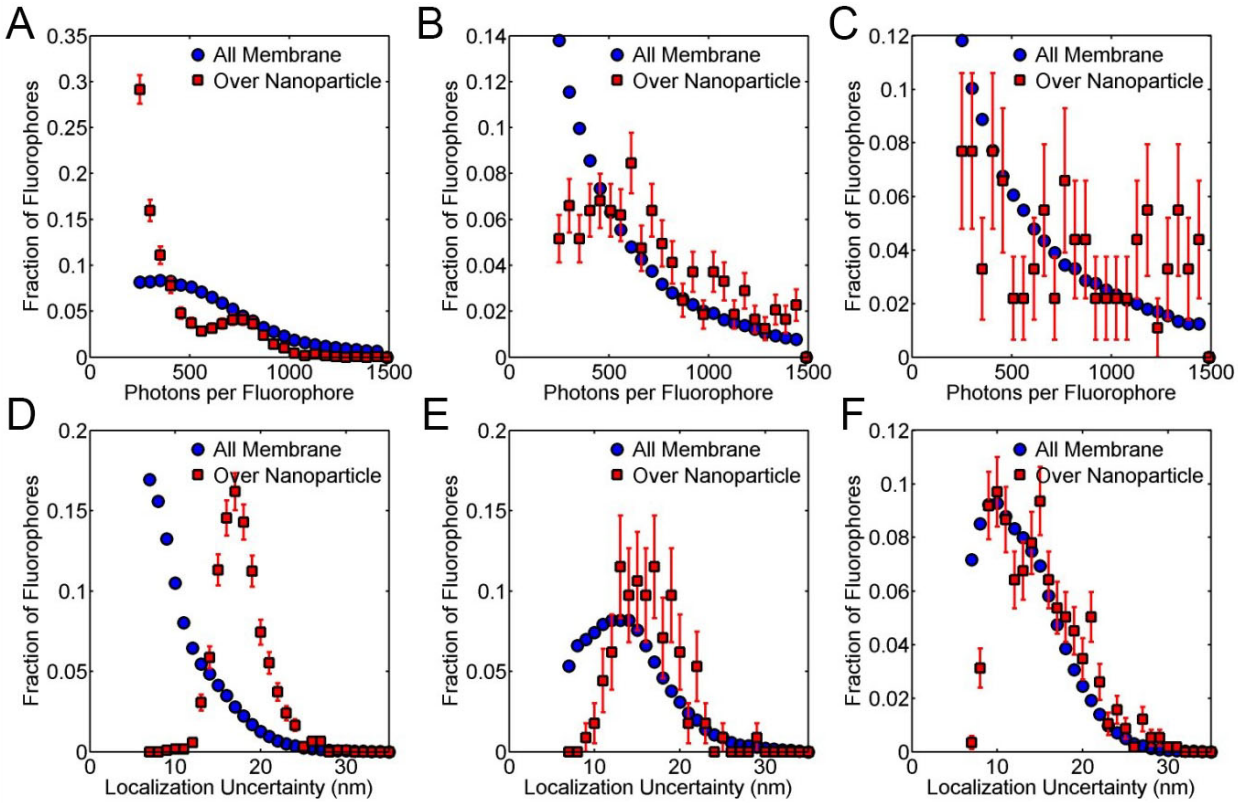

FIGURE S3 The distribution of the number of photons per fluorophore obtained from pPLM data of the whole membrane in comparison to the detections from the curvature region and the corresponding localization uncertainty for membrane over 24 (A,D), 51 (B,E), and 70 (C,F) nm radius nanoparticles.

	Curved or Flat Membrane	Number of Photons per Fluorophore	Localization Precision (nm)
pPLM	$r < 150$ nm	890 ± 260	16.0 ± 1.5
	$r > 150$ nm	840 ± 130	12.5 ± 1.5
sPLM	$r < 150$ nm	720 ± 180	13 ± 3
	$r > 150$ nm	810 ± 140	11 ± 3

Table S1 PLM depends on the localization of each blinking fluorophore by finding the center of the image of an isolated fluorophore. The reported uncertainty of each value is the standard deviation of the measured values.

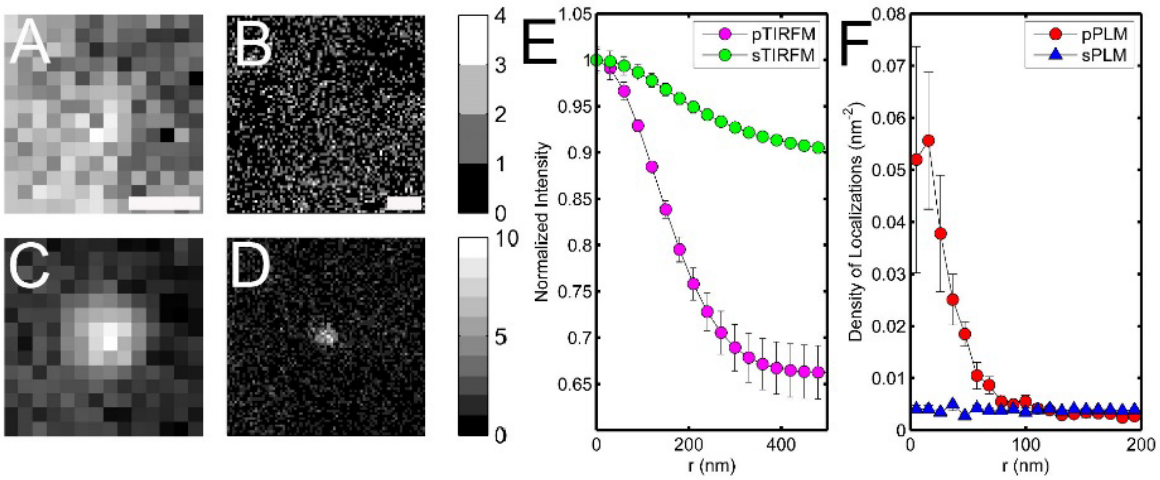

FIGURE S4 Membrane curvature detection over 24 nm radius NPs. (A, C) Diffraction-limited sTIRF and pTIRF, respectively. (B, D) Super-resolution reconstructed images of sPLM and pPLM, respectively. Average radial line scans (E) for TIRM and average radial density line scan (F) for PLM are for membrane over 10 NPs events of r_{NP} of 24 nm. (E) The diffraction-limited PSF limits the ability to identify the size of each event. Error bars represent fitting uncertainty to 95% confidence bounds. (F) PLM provides improved resolution in the sensitivity of detecting nanoscale curvature. Error bars represent standard error of the mean. Scale bar in (A, C) represents 200 nm. Scale bar in (B, D) represents 100 nm.

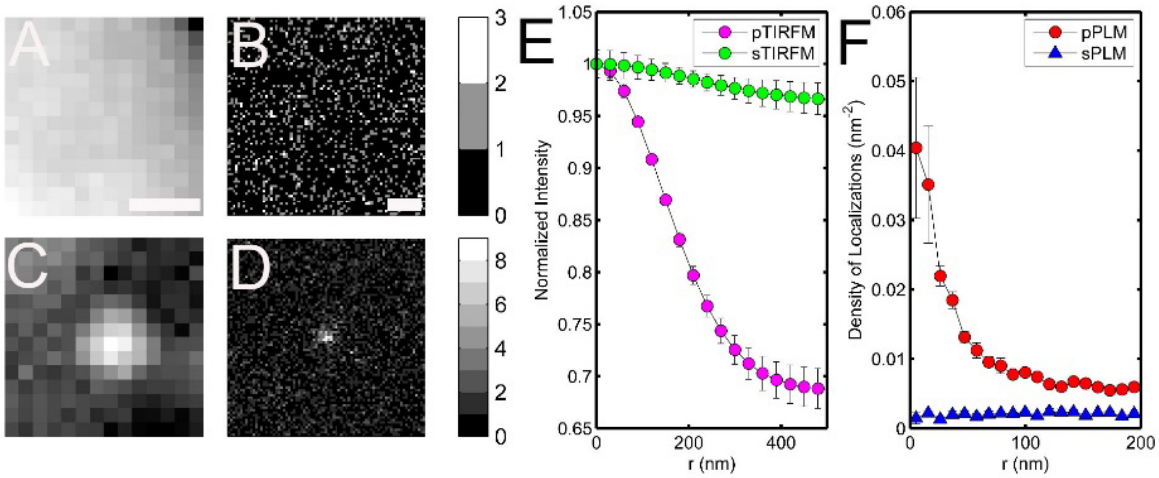

FIGURE S5 Membrane curvature detection over 51 nm radius NPs. (A, C) Diffraction-limited sTIRF and pTIRF, respectively. (B, D) Super-resolution reconstructed images of sPLM and pPLM, respectively. Average radial line scans (E) for TIRM and average radial density line scan (F) for PLM are for membrane over 10 NPs events of r_{NP} of 51 nm. (E) The diffraction-limited PSF limits the ability to identify the size of each event. Error bars represent fitting uncertainty to 95% confidence bounds. (F) PLM provides improved resolution in the sensitivity of detecting nanoscale curvature. Error bars represent standard error of the mean. Scale bar in (A, C) represents 200 nm. Scale bar in (B, D) represents 100 nm.

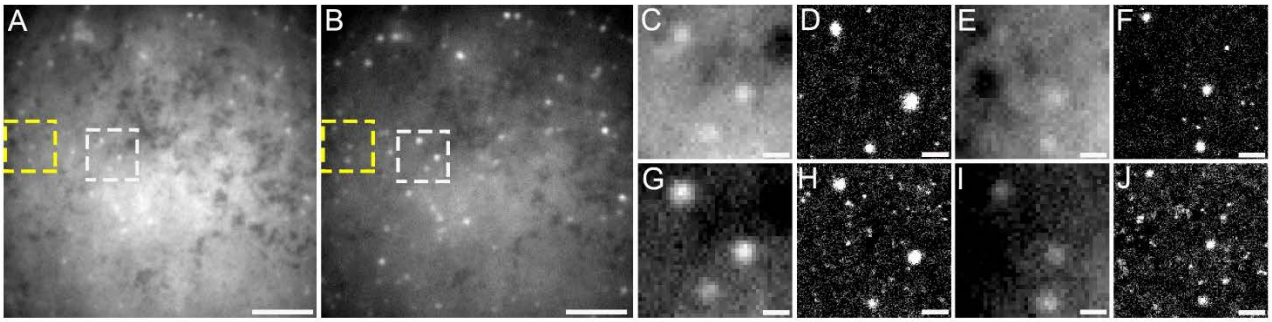

FIGURE S6 Membrane curvature detection of LUVs on an SLB. (A-C, E, G, I) Diffraction-limited polarized TIRFM images and (D, F, H, J) PLM images of a POPC/Biotin/DiI membrane with unfused LUVs where the excitation light was s-polarized in (A, C-F) or p-polarized in (B, G-J). (C-F) and (G-J) are magnified images for regions within the white and yellow box, respectively. Scale bars represent (A, B) 5μm, (C-J) 200 nm.

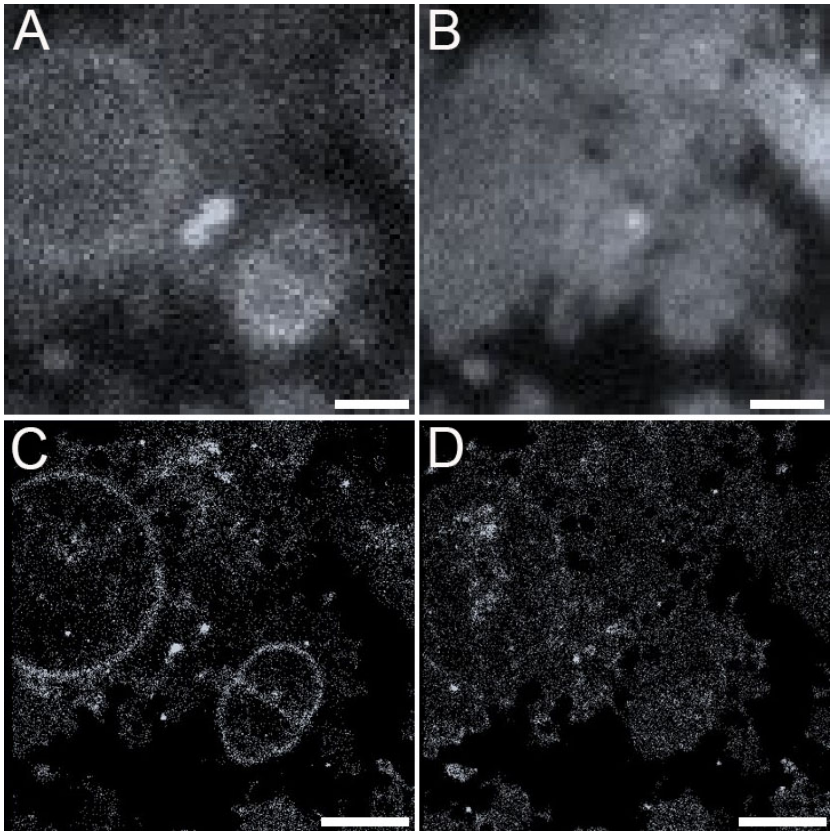

FIGURE S7 Polarized Localization Microscopy detects the vertical edge of GUVs adhered to an SLB. (A) Diffraction-limited pTIRFM image of the supported lipid bilayer and the GUVs shows an increase in brightness corresponding to the vertical edge of the GUV. Black region is glass surrounding the labeled lipid membrane. (B) The uniform fluorescence in the diffraction-limited sTIRFM image indicates the presence of membrane with no specificity to membranes of varying orientation. (C) 2D histogram plot of localizations from pPLM demonstrates the increased density of localizations from vertical membranes. The vertical edge membrane perpendicular to the glass is clearly observed within the super-resolution image, in addition to the membrane between the two adjacent GUVs. (D) Histograms of localization in sPLM demonstrate a more uniform distribution of localizations. Scale bars represent 1μm.

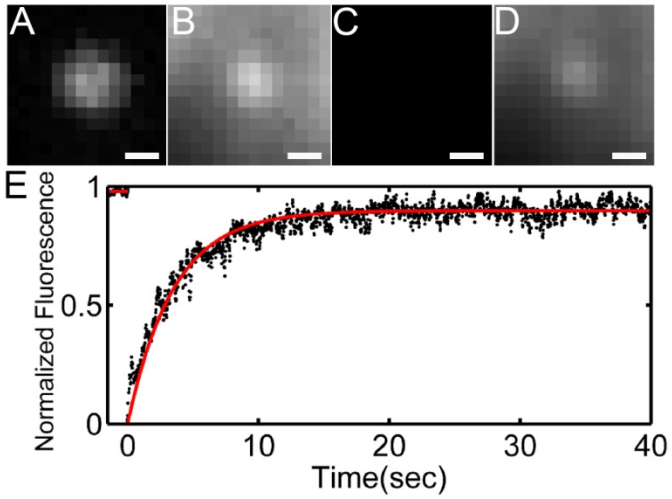

FIGURE S8 Membrane draped over the nanoparticle is intact, uniform, and continuous over the nanoparticle, and extend over to the glass coverslip. Upon performing FRAP analysis, lipids were observed to diffuse and exchange with unbleached lipids from the surrounding membrane directly on the coverslip. (A) Fluorescence image of the 24 nm radius nanoparticle with λ_{ex} = 647 nm. (B-D) Fluorescence image of POPC:DiI membrane with λ_{ex} = 561 nm (B) before, (C) immediately after, and (D) 40 s after bleaching. (E) FRAP result of a 100 μm^2 of membrane overlaying sporadic nanoparticles demonstrates the bulk 0.3 ± 0.1 $\mu m^2/s$ diffusion coefficient.

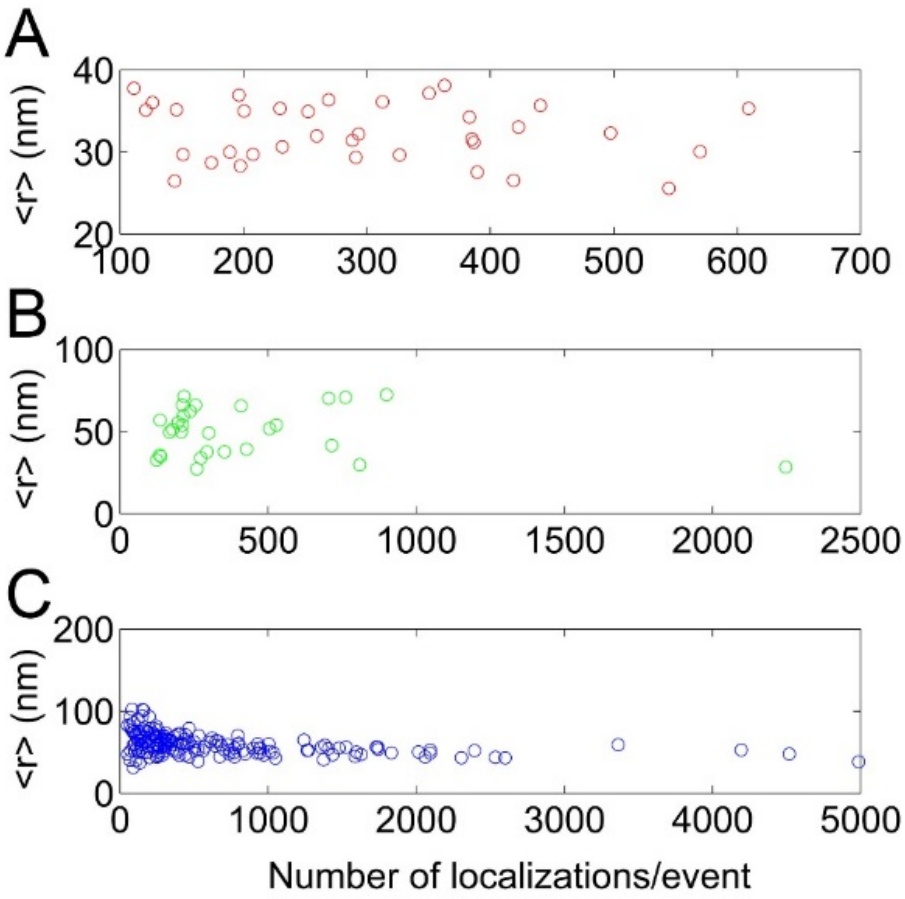

Figure S9 The number of localization obtained per curvature event induced by NPs. The higher the number of localizations/event, the more confidence in <r> is obtained. (A-C) Calculated <r> versus the number of localizations/event for r_{NP} = 24, 51, and 70 nm, respectively.

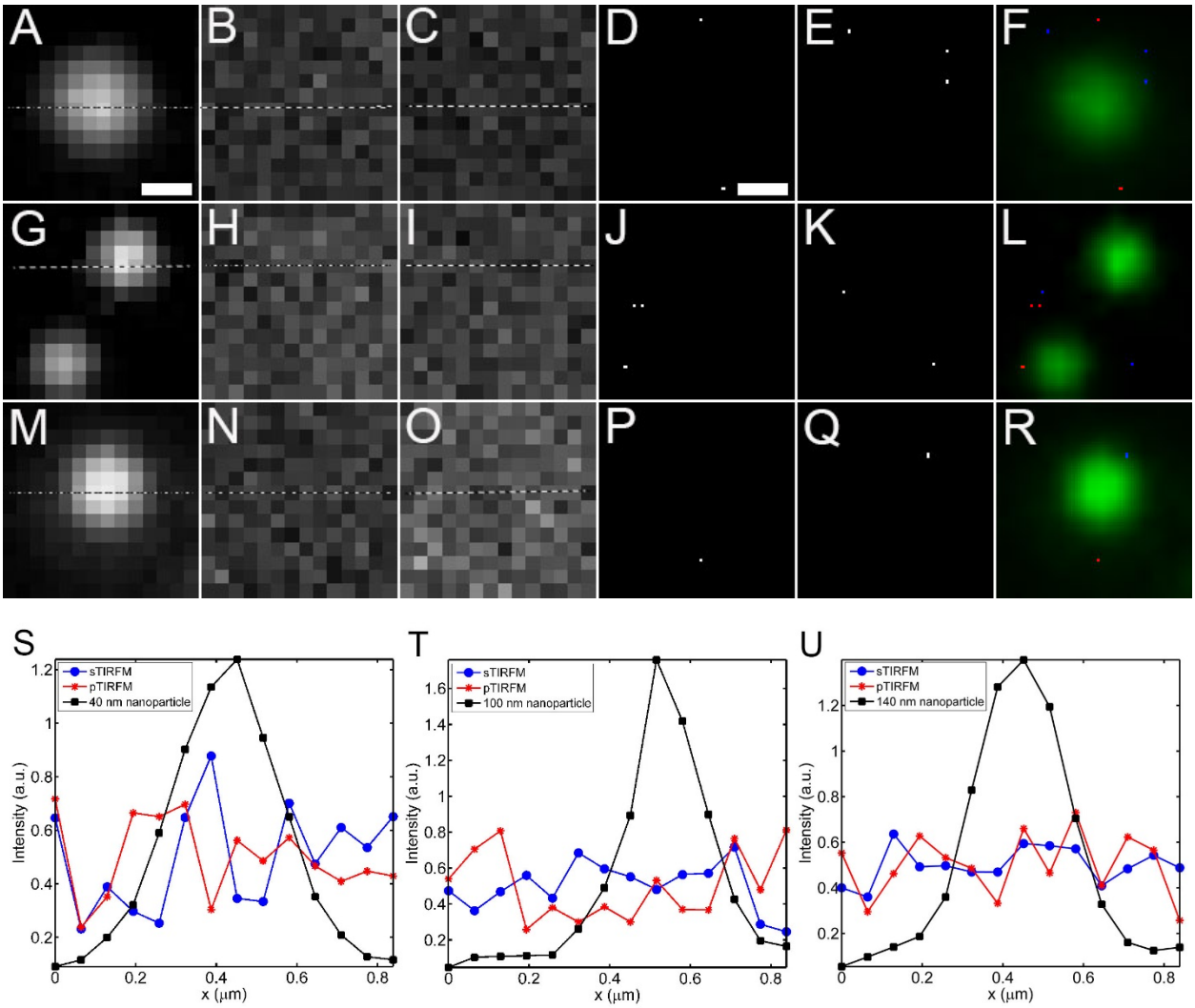

FIGURE S10 The fluorescent nanoparticles are not detected or localized in the 561 nm channel. As a control experiment, fluorescent nanoparticles on the glass in the absence of a DiI were imaged and analyzed with the same experimental conditions as typically done for PLM. Imaged nanoparticles have radii of 24 nm (A-F, S), 51 nm (G-L, T), and 70 nm (M-R, U), with primary excitation/emission wavelengths ($\lambda_{ex}/\lambda_{em}$) of 647nm/680nm, 488nm/508nm, and 405nm/515nm, respectively. No significant localizations were collected at the site of the nanoparticles in the absence of DiI. (A, G, M) Diffraction-limited fluorescence images of the nanoparticles. (B, H, N) Diffraction-limited pTIRFM with $\lambda_{ex}/\lambda_{em}$ = 561nm/600nm. (C, I, O) Diffraction-limited sTIRFM with $\lambda_{ex}/\lambda_{em}$ = 561nm/600nm. (D, J, P) pPLM with $\lambda_{ex}/\lambda_{em}$ = 561nm/600nm. (E, K, Q) sPLM with $\lambda_{ex}/\lambda_{em}$ = 561nm/600nm. (F, L, R) Color merge for nanoparticles (green), localizations in sPLM (blue), and pPLM (red). Scale bars represent 200 nm.

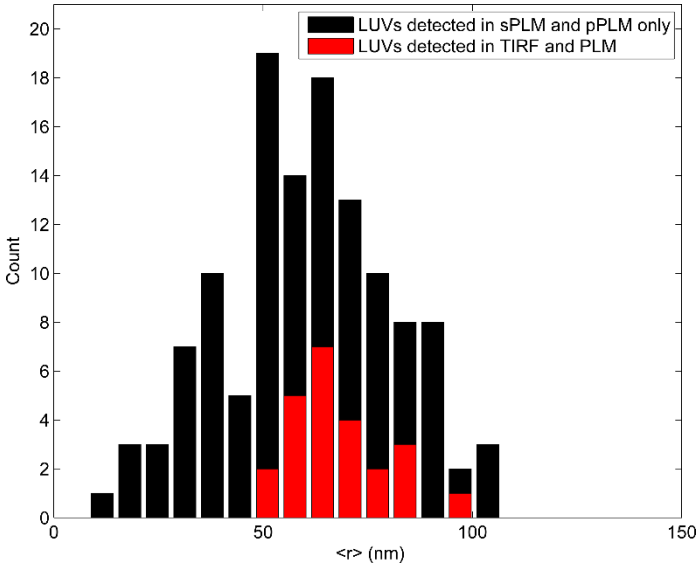

FIGURE S11 The increased probability of detecting LUVs in PLM versus TIRF for each LUV size. PLM not only detects and resolves the sizes of LUVs observed in TIRF, but it also detects LUVs unseen in TIRF. A histogram of LUV sizes (<r>) for LUVs detected only in sPLM and pPLM but not in TIRF shown in black, the mean size is 62 ± 20 nm. The red histogram represents a subset of the LUVs detected in PLM but also observed in p-polarized and s-polarized TIRF, the mean size is shifted to larger values of <r> = 72 ± 10 nm.

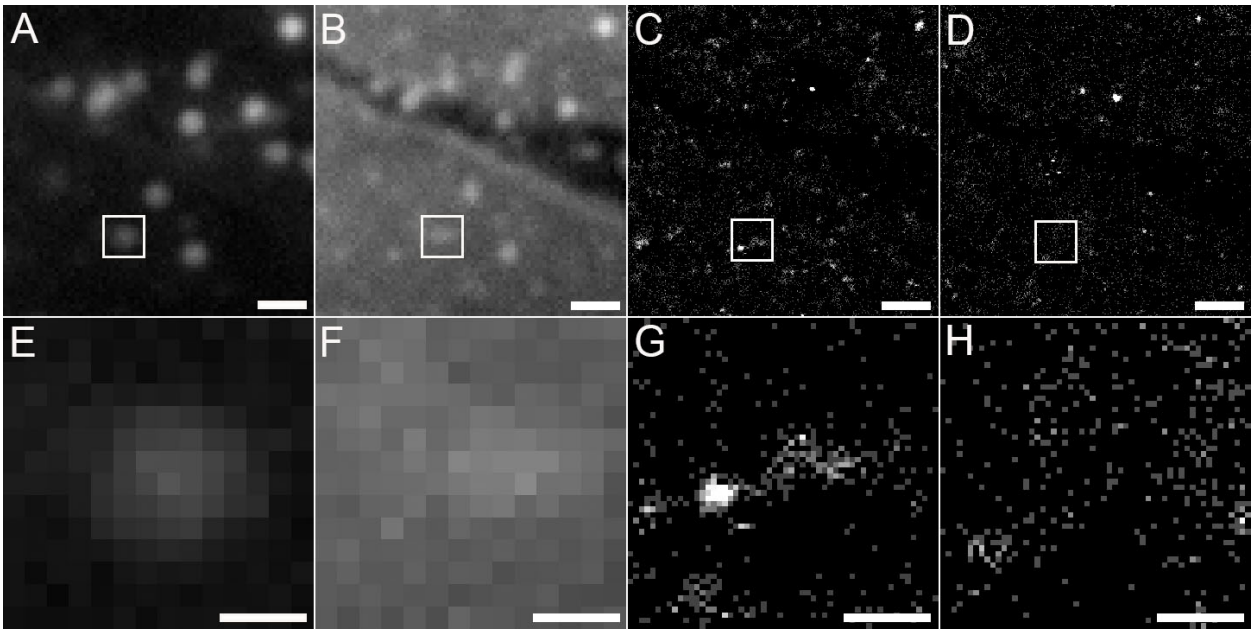

FIGURE S12 In the absence of biotin-streptavidin binding, LUV diffused on the SLB, which proved to be problematic when resolving the LUV size via PLM. A 'tail' of localizations is detected as the LUV diffused across the SLB. (A) Diffraction-limited pTIRFM image of the membrane, the white box labels the LUV location. The increase in brightness in the pTIRFM image indicates the presence of curved membrane. Black region is glass. (B) Diffraction-limited sTIRFM image, the uniform brightness within the white box indicates the presence of membrane. (C) Histograms of localizations in pPLM, the increased density of localizations indicate the presence of membrane curvature. The region to the right of the central bright pixels in (G) shows a lower density of localizations as the LUV diffused through this area. (D) Histograms of localization in sPLM demonstrate a more uniform distribution of localizations and the presence of membrane. (E-H) are zoomed in regions for marked white boxes in (A-D) respectively. Scale bars represent (A-D) 3μm, and (E-H) 300 nm.

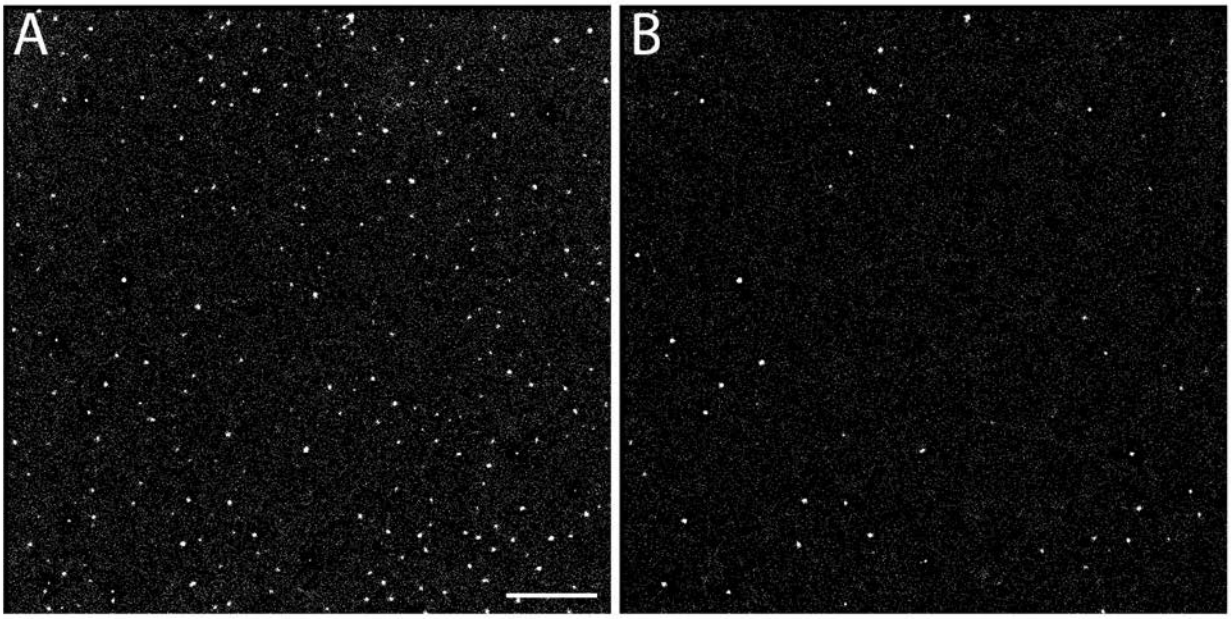

FIGURE S13 Membrane curvature generated by draping a supported lipid bilayer on r_{NP} = 70 nm NPs. Reconstructed images of the membrane presented as 2D histograms of the localizations in (A) pPLM and (B) sPLM, respectively. The scale bar represents 5µm.

REFERENCES

1. Veatch, S. 2007. Electro-Formation and Fluorescence Microscopy of Giant Vesicles With Coexisting Liquid Phases. In: McIntosh T, editor. Lipid Rafts. Humana Press. pp. 59–72.

2. Shim, S.-H., C. Xia, G. Zhong, H.P. Babcock, J.C. Vaughan, B. Huang, X. Wang, C. Xu, G.-Q. Bi, and X. Zhuang. 2012. Super-resolution fluorescence imaging of organelles in live cells with photoswitchable membrane probes. Proc. Natl. Acad. Sci. U. S. A. 109: 13978–13983.

3. Dempsey, G.T., M. Bates, W.E. Kowtoniuk, D.R. Liu, R.Y. Tsien, and X. Zhuang. 2009. Photoswitching mechanism of cyanine dyes. J. Am. Chem. Soc. 131: 18192–18193.

4. Lew, M.D., M.P. Backlund, and W.E. Moerner. 2013. Rotational mobility of single molecules affects localization accuracy in super-resolution fluorescence microscopy. Nano Lett. 13: 3967–3972.

5. Agrawal, A., S. Quirin, G. Grover, and R. Piestun. 2012. Limits of 3D dipole localization and orientation estimation for single-molecule imaging: towards Green's tensor engineering. Opt. Express. 20: 26667–26680.